Conformation-dependent influences of hydrophobic amino acids in two in-register parallel β-sheet amyloids, an α-synuclein amyloid and a local structural model of PrP^{Sc}

Hiroki Otaki,[*,†,¶] Yuzuru Taguchi,[*,‡,¶] and Noriyuki Nishida[‡]

†*Center for Bioinformatics and Molecular Medicine, Graduate School of Biomedical Sciences, Nagasaki University, 1-14 Bunkyo-machi, Nagasaki 852-8521, Japan*

‡*Department of Molecular Microbiology and Immunology, Graduate School of Biomedical Sciences, Nagasaki University, 1-12-4 Sakamoto, Nagasaki 852-8523, Japan*

¶*Contributed equally to this work*

E-mail: otaki@nagasaki-u.ac.jp; ytaguchi@nagasaki-u.ac.jp

Abstract

Prions are unconventional pathogens that encode the pathogenic information in conformations of the constituent abnormal isoform of prion protein (PrP^{Sc}), independently of nucleotide genome. Therefore, conformational diversity of PrP^{Sc} underlies the existence of many prion strains and species barriers of prions, although the conformations still remain undetermined. Interestingly, differences between polymorphic or species-specific residues responsible for the species/strain barriers are often caused by conservative replacements between hydrophobic amino acids. This implies that subtle differences among hydrophobic amino acids are significant for PrP^{Sc} structures. Here, we analyzed the influence of different hydrophobic residues on the structures of an

in-register parallel β-sheet amyloid of α-synuclein (αSyn) using molecular dynamics (MD) simulation, and applied the knowledge from the αSyn amyloid to modeling local structures of human PrP^{Sc} encompassing residues 107–143. We found that mutations equivalent to polymorphisms that cause transmission barriers substantially affect the stabilities; for example, the G127V mutation, which makes the host resistant to various human prion diseases, greatly destabilized the amyloid. Our study demonstrates specifically how and in what structures hydrophobic residues can exert unique effects on in-register parallel β-sheet amyloids and provides insights into the molecular mechanism of the strain diversity of prions and other pathogenic amyloids.

1 Introduction

Prion diseases are a group of neurodegenerative disorders that are characterized by the accumulation of the abnormal isoform (PrP^{Sc}) of prion protein (PrP) in the central nervous system.[1] Prion diseases have three etiologies, sporadic, inherited, and acquired, depending on how the causative PrP^{Sc} propagation is initiated in the body. In sporadic and inherited prion diseases, for example, sporadic Creutzfeldt-Jakob disease (CJD) and fatal familial insomnia (FFI), respectively, the causative PrP^{Sc} are generated by the spontaneous conformational conversion of endogenous normal isoform PrP (PrP^{C}) into PrP^{Sc}, with or without the aid of pathogenic mutations in the *PRNP* gene. Acquired prion diseases are caused by the intake of exogenous PrP^{Sc} as infectious prion agents, such as epidemic bovine spongiform encephalopathy (BSE) in cattle[2] and chronic wasting disease (CWD) in cervids.[3] Prions behave similarly to viruses, with high infectivity, the existence of many strains, species/strain barriers, and adaptation to new hosts, despite the lack of conventional genetic material. These virus-like pathogenic properties of prions are hypothesized to be enciphered in the conformations of PrP^{Sc}, a theory known as the protein-only hypothesis.[1,4]

Indeed, the pathogenic properties of prions and the consequent clinical phenotypes are greatly affected by the primary structure of constituent PrP^{Sc}, which is consistent with

the fundamental fact that the conformations of proteins are determined by their primary structures. For example, in sporadic CJD, PrP deposition patterns, lesion profiles in the brain, clinical presentations, and the apparent molecular sizes of protease-resistant cores of PrP^{Sc} vary depending on whether the polymorphic codon 129 is methionine (M129) or valine (V129).[5] A pathogenic mutation D178N of human PrP causes either FFI or familial CJD in association with M129 or V129, respectively.[6] The vast majority of the new-variant CJD cases, which resulted from the trans-species transmission of BSE to humans, have been homozygous for M129.[7,8] Moreover, the methionine/leucine polymorphism at codon 132 of elk PrP, which is equivalent to the codon 129 polymorphism of human PrP, also affects the susceptibility to CWD.[9,10] From the viewpoint of the protein-only hypothesis, polymorphisms could affect the stability of PrP^{C}, and should also affect disease susceptibility through structural alterations of the constituent PrP^{Sc}; however, the specific manner in which the subtle differences between those hydrophobic amino acids affect the structures of PrP^{Sc} has not been identified yet. Detailed structures of PrP^{Sc} will be needed for such investigation, but with all currently available data, even whether PrP^{Sc} is an in-register parallel β-sheet amyloid or a β-solenoid is still controversial due to its incompatibility with conventional high-resolution structural analyses.[11–18]

In addition to induction by the methionine/valine polymorphic codon 129, strain/species barriers of prions can also be caused by conservative replacements between different hydrophobic amino acids at other residues. In experiments with a C-terminally-truncated Y145Stop mutant of human PrP and the counterparts in mouse and Syrian hamster PrPs, whether residue 138 or 139 (in human numbering throughout, unless otherwise noted) was isoleucine or methionine was critical for efficient amyloid formation and cross-seeding among them.[19,20] In the transmission of the prions of sporadic CJD homozygous for M129 to transgenic mice expressing human-mouse chimeric PrP, I138M substitution substantially extended the incubation periods.[21] Different hydrophobic amino acids at codons 109 and 112 influenced the transmission efficiencies of prions among different hamster species.[22,23] In in vitro

cross-seeding between ovine PrP and cervine CWD, an I208M (in ovine numbering) mutation showed a profound influence on the seeding efficiencies.[24] Given these documented facts, we are interested in the effect of different hydrophobic residues on the structures of amyloids, particularly whether methionine has unique properties compared with other hydrophobic amino acids. Amyloids of Y145Stop mutant of human PrP that have in-register parallel β-sheet structures[16,18,25,26] were reported to induce PrP^{Sc} in the inoculated mice and caused bona fide prion diseases,[27] suggesting that the amyloids may have similar structures with the pathogenic PrP^{Sc}. We thus used an in-register parallel β-sheet amyloid of α-synuclein (αSyn) as a surrogate local structural model for PrP^{Sc}, as in our previous studies.[28,29]

αSyn amyloid is the main component of Lewy bodies, which is a hallmark of Parkinson's disease and dementia with Lewy bodies (DLB), and reportedly has prion-like properties which include transmissibility and strain diversity.[30] For instance, αSyn forms various types of amyloids in vitro, which are different in appearance, proteolytic fragment patterns, and cytotoxicity.[31] Moreover, αSyn amyloids isolated from DLB and multiple system atrophy had different proteolytic fragment patterns suggestive of distinct conformations.[32] These findings are highly reminiscent of prions and imply that prion-like properties are inherent in in-register parallel β-sheet structures. Detailed structures of αSyn amyloids have been determined with solid-state NMR (ssNMR)[33] or cryo-electron microscopy (cryo-EM);[34,35] thus we used a Greek-key αSyn amyloid (PDB ID: 2N0A;[33] Figure 1) to investigate the effects of different hydrophobic residues on the in-register parallel β-sheet structures. Our studies have revealed that the lengths and C_β-branching of the side chains of hydrophobic residues are important for the stability of local amyloid structures, particularly in a U-shaped β-arch. Next, we applied the knowledge from the αSyn amyloid to a local structural model of PrP^{Sc} encompassing residues 107 to 143 of human PrP, $PrP_{107\text{-}143}$, assuming that PrP^{Sc} was also an in-register parallel β-sheet amyloid. We assessed how mutations and polymorphisms associated with the strain diversity of prions affected the structures of the model amyloid using molecular dynamics (MD) simulation. Our studies have demonstrated specifically how

different types of hydrophobic amino acids affect the structures of in-register parallel β-sheet amyloids of αSyn and $PrP_{107\text{-}143}$. We have also found that the structural stability of U-shaped β-arches requires hydrophobic cores with well-balanced interactions among the constituent hydrophobic residues. Knowledge from the present study will advance our understanding of the strain diversity of amyloids and facilitate the design of more plausible PrP^{Sc} models and other amyloids in the future.

2 Results and Discussion

2.1 Investigation of the mechanism by which G84M mutation stabilizes the αSyn amyloid

In a previous study, we compared the effects of isoleucine substitutions at residues 61 (E61I) in a flat-loop (loop(57–62)) and 84 (G84I) in a U-shaped loop (loop(84–87)) in the αSyn amyloids.[28] We showed that the G84I mutant substantially destabilized the U-shaped loop, whereas the E61I mutant had little influence on the stability of αSyn amyloid. Here, we investigated the influences of hydrophobic amino acids on the local structures of αSyn amyloids by introducing methionine substitutions at the same positions (E61M and G84M). Figure 2A shows the final snapshots of MD simulations of αSyn amyloids, and Figure 2B shows the heatmaps of the β-sheet propensity. The MD simulations of homo-oligomer amyloids of αSyn(E61M) and αSyn(G84M) revealed that both the mutations tended to stabilize the local structures, particularly when these amyloids induced new β-sheets in the flat-loop for the E61M mutant, or U-shaped loop for the G84M mutant (Figure 2A). This stabilization in αSyn(E61M) could be interpreted as the effects of the charge difference in the E61M mutation: side chains of M61 formed hydrophobic contacts with those of the neighboring chains along the stacking direction in the E61M mutant, whereas negative charge of glutamate hampered the stabilization between the neighboring chains in the WT. Overall, the influence of the methionine substitution (E61M) was similar to those of the isoleucine

substitution (E61I) in the flat-loop.

The effects of the G84M substitution were more impressive : almost the entire region C-terminal to residue 80, including loop(84–87), was converted to stable β-sheets, in contrast to those of G84I substitution.[28] We thus further compared the substitution effect of G84M, G84L, G84V, and G84I. In the G84L mutant (αSyn(G84L)), the loop region around L84 was substantially destabilized like that of αSyn(G84I).[28] A G84V mutant (αSyn(G84V)) also shows β-sheet propensity similar to that of αSyn(G84L). Being interested in the opposite effects of G84M and G84L/V/I, we focus on residue 84 to identify the underlying mechanisms.

Directions of the side chains of αSyn(G84M) and αSyn(G84L) are compared in the insets of Figure 2A. The final status of 400-ns simulations was different between the αSyn(G84M) and αSyn(G84L) amyloids. All the side chains of methionine at residue 84 (M84) pointed inward of loop(84–87) and were close to those of V82 and A89, whereas some side chains of leucine at residue 84 (L84) flipped and pointed outward.

The hydrophobic contact diagrams are shown in Figure 3. The diagrams of the αSyn(G84M), αSyn(G84L), αSyn(G84V), and αSyn(G84I) amyloids clearly exhibited differences. M84 of αSyn(G84M) amyloid had intra-chain interactions evenly with residues 82 and 89 in all the layers, and the interactions were reproducible. In contrast, αSyn(G84L) and αSyn(G84V) amyloids only infrequently showed that pattern or were similar to those of another destabilizing mutation, G84I.[28] This result was reflected in the distance between residues 84 and 89. The C_α-C_α distances (dC_α) between the residues 84 and 89 were about 8.3 Å in all the chains during the simulations of αSyn(G84M), whereas the distances varied among chains and fluctuated in αSyn(G84L), αSyn(G84V), and αSyn(G84I) (Figure S1).

The unique stabilizing effects of M84 would be attributable to the long side chain, which can extend across the β-arch like a crossbeam. During the simulation, the ends of the side chains were fixed in the proximity of A89 (Movie S1). The intimate interactions with A89 reinforced the hydrophobic core and stabilized the β-arch. Leucine could not replace methionine despite their similarity in hydrophobicity and non-branching C_β atom, because

its side chain is not long enough for stable interactions with A89. Indeed, experiments have confirmed that the subtle difference between methionine and leucine is significant in certain cases of prion propagation, as the methionine/leucine polymorphism of elk PrP affects the susceptibility to CWD infection.[9,10] The local structures of CWD-PrP^{Sc} around the polymorphic residue might be similar to the U-shaped loop of αSyn—that is, the long side chain of methionine is essential for stability.

2.2 Modeling a local structure of PrP^{Sc} based on knowledge from the αSyn amyloids

Given the knowledge from our studies on αSyn amyloids,[28,29] we attempted to model a local structure of PrP^{Sc} with a U-shaped loop. A region comprising a glycine-rich motif encompassing residues 123–127 of human PrP ($-GGL_{125}GG-$) seems to be suitable for a U-shaped loop. In addition, the anti-prion effect of valine at residue 127 against various sporadic CJD[36] is reminiscent of the destabilizing effects of V84 in the αSyn amyloid, which suggests the presence of a U-shaped loop in the region. Moreover, structures of amyloid cores of Y145Stop-mutant PrP investigated with ssNMR are available, although not in atomic resolution.[16,25] Amyloids of the Y145Stop-mutant induced infectious PrP^{Sc} that caused bona fide prion disease when inoculated into mice,[27] and could therefore share similar local structures with full-length PrP^{Sc}. We thus tentatively modeled local structures of PrP^{Sc} in region 107–143, $PrP_{107\text{-}143}$, utilizing the structural model of the Y145Stop mutant propounded by Theint et al.[25] and the knowledge from the αSyn amyloid for stable β-arches (Figure 4A). Although a rather distinct structural model based on cryo-EM was recently reported,[37] the particular amyloid was not demonstrated to cause prion disease in mice and we did not adopt it. To sample the conformational space of $PrP_{107\text{-}143}$ more broadly, we conducted 10 independent 50-ns MD simulations for the wild-type (WT). Although the stack ends of the model amyloid (chains A and J) were not very stable as expected, as a whole our model was sufficiently stable during 50-ns MD simulations (Figures 4B and S2A, see also Movie

S2). We then modeled mutants of $PrP_{107\text{-}143}$ (G127V, M129V, I138M, M129V&I138M, and A133V) and performed 10 independent 50-ns MD simulations. The results are discussed in the following sections.

2.3 Influence of G127V mutation on the $PrP_{107\text{-}143}$ amyloid

Final snapshots of MD simulation for the G127V mutant, $PrP_{107\text{-}143}$(G127V), are presented in Figure 4C, from which we confirmed the destabilizing effects of the mutation on the U-shaped loop (residues 120–130; see also Movie S3). These effects are reflected in the root-mean-square fluctuation (RMSF) of C_α atoms and β-sheet propensity values shown in Figure 5: the heatmaps of $PrP_{107\text{-}143}$(G127V) indicate the disorder around the U-shaped loop. To validate the (in)stability of the modeled amyloids, we introduced a novel parameter, proximity score, which represent the sum total of the persistence of the hydrophobic contacts between two hydrophobic residues over the 10 chains, A–J (Figure S3A). The score counts hydrophobic contacts between the two residues of interest irrespective of intra- or inter-chain interactions and presumably indicates total contribution of these residues to the stability of the amyloid. Unlike traditional contact maps, we can set threshold for the contact so that the score reflects the stability of the system. Here, threshold for the hydrophobic contact was set at 5 Å,[38] because typical distance between neighboring β-strands within a β-sheet is 4.8 Å. The scores correlated with distances between the two corresponding residues in certain cases (Figure S3B) and reflected the stability of the hydrophobic cores. The proximity score would be advantageous in evaluating interactions in amyloids. Additionally, the score enabled us to statistically compare the hydrophobic interaction of each residue pair. Figures 6 and 7 summarize the proximity scores in the U-shaped loop and the N-/C-terminal-side regions, respectively. The proximity scores for V122-V122, L125-L125, and L130-L130 of $PrP_{107\text{-}143}$(G127V) significantly decreased compared with those of the WT. The score for V122-M129 also decreased, although not to a statistically significant degree. These results indicate that those residues are frequently wide apart, consistent with disordered U-shaped

loops. In the other regions, the proximity scores for A115-V121, A118-A133, and A118-P137 decreased, although not statistically significant, either. Destabilization of the amyloid structure caused by the G127V mutation is consistent with the protective effects of a V127 polymorphism of human PrP against CJD transmission,[36] because the destabilization would abolish propagation of the PrP^{Sc} in the brain.

2.4 Influence of M129V mutation on the $PrP_{107\text{-}143}$ amyloid

Next, we analyzed the influence of M129V substitution, which is equivalent to V129 polymorphism of human PrP, on the stability of the hydrophobic cores. The mutant amyloid, $PrP_{107\text{-}143}$(M129V), appeared more stable during the 50-ns simulation than the WT (Figure 4D). Comparison of their RMSF and β-sheet propensity values between the WT and M129V validated the stability, with more demarcated loops (residues 116–119, especially chains A–E) and more stable β-sheets (residues 120–122 and 128–133) (Figure 5).

Proximity scores of the WT and the mutant revealed more detailed differences. Most notable was the alteration in the balance of interactions between A120, V122, L125, and V129 in the hydrophobic cores of the U-shaped loops (Figure 6). The WT showed outstandingly high proximity scores for V122-M129 ($\sim$ 600) in the U-shaped loop, whereas the M129V mutation reduced the score (to about 400) and, instead, increased the scores for A120-V129 (to about 600) and V122-L125 (to about 500) . The higher scores for A120-A120 and V129-V129 reflected the greater structural stability of the mutant amyloid. The mutation also affected interactions in remote regions, as demonstrated by the significant decreases of the proximity score for A118-P137 (Figure 7). Some increases of the proximity scores were also seen, for example, those for A113-V121, A117-A133, A117-I139, A118-A133, and I139-I139, although they were not statistically significant. The altered interactions in the N-terminal-side region (A113-V121 and A115-V121) are particularly interesting, because they are located on the other side from V129 across β-strand 120–122 and do not directly contact V129. Presumably, the dynamics of the β-sheet(120–122) were initially affected by

the mutation, subsequently altering the interaction patterns of V121.

It should be noted that the above description applies to M129V&I138M mutant, and some interactions are enhanced by the I138M mutation. As shown in Figure 4D, the distance between β-sheet(120–122) and β-sheet(128–133) seems to be narrower in the M129V mutant. Indeed, the M129V mutation increased the proximity scores for A118-A133 (Figure 7), and the distances between the C_α atoms of A118 and S132, dC$_\alpha$(A118–S132), tended to be shorter in mutants with M129V mutations (Figure 8A, green and blue squares) than in the WT (red dots). Interestingly, the WT and mutants with M129 mostly had shorter dC$_\alpha$(A118–A/V133) than dC$_\alpha$(A118–S132), whereas the two distances of the V129 mutants (M129V and M129V&I138M) were comparable (Figure 8B). Figure 8C presents a correlation between dC$_\alpha$(A120–M/V129) and dC$_\alpha$(A118–S132). The mutants with V129 showed obviously shorter dC$_\alpha$(A120–M/V129) than those with M129. Additionally, in the mutants with V129, the distances between C_α atoms of A120 and V129, dC$_\alpha$(A120–V129), were shorter than dC$_\alpha$(V122–V129); while the others showed the opposite tendency (Figure 8D). All these findings are explainable by assuming an "upward" positional shift of the β-sheet(128–133) in the mutants with V129 (Figure 8E,F) that is attributed to the side chain of V129 being shorter than that of M129. This shortness enabled V129 to further approach toward A120 and consequently caused well-balanced interactions of the hydrophobic residues and closer positioning of the two β-sheets. In addition to the local effects, the positional shift also expanded the range of motion of the C-terminal-side region, leading to a significant loss of interaction for A118-P137 and facilitating interactions of A116-F141 and A117-I139 (Figure 7). In contrast, with the long side chain of M129, the biased interactions with V122 seemed to hamper the approach of residue 129 toward A120 (Figure 6).

2.5 Influence of I138M mutation on the $PrP_{107\text{-}143}$ amyloid with or without M129V mutation

Residue 138 is one of the residues that are often varied between species, for example, this residue is isoleucine in humans, methionine in many rodents, and leucine in many ruminants. Moreover, this residue is the most influential on the mouse-human species barrier in the transmission of sporadic CJD[21] and also in the cross-seeding of Y145Stop peptides of human and mouse PrP.[20] We assessed how the I138M mutation affected the local structural model of PrP^{Sc}. The most remarkable finding is the tendency of the C-terminal-side region to lean over toward the N-terminal-side region (Figure 4E), presumably due to bending at the loop(134–137). Because of the bending, the angle between the β-sheet(128–133) and the β-sheet(139–141) appeared to be near-square to acute in many runs of the I138M mutants, particularly in $PrP_{107\text{-}143}$(M129V&I138M), whereas the WT or other mutants tended to have obtuse angles (Figures 4 and S2).

In a comparison between the I138M mutants and the WT, the RMSF, the β-sheet propensity, and the proximity scores were similar, but interestingly, the proximity scores for A133-P137 were higher in the I138M mutants, although not significant (Figures 5, 6, and 7). Figure 9 represents the proximity scores for A133-P137 of each MD run. The scores of 10 independent MD runs showed dispersed values in each mutant. However, the scores for A133-P137 of nine runs were higher than 200 in $PrP_{107\text{-}143}$(M129V&I138M), whereas three or four runs in the other mutants. In the runs with relatively high proximity scores for A133-P137, the amyloids tended to form small loops like an Ω-shape (Figure 4F). This loop is encompassing A133 and P137 and has near-square to acute angles between the β-sheet(128–133) and the β-sheet(139–141), irrespective of the primary structures (see boxed snapshots in Figure S2). For example, the final snapshot of Run 7 of $PrP_{107\text{-}143}$(M129V) (Figure 4D), which has an Ω-shaped loop(134–137), also had a high proximity score (417.7, Figure 9).

The deeper bending of the loop, even to acute angles caused by the I138M mutation, would be attributable to the high intrinsic α-helix propensity of methionine [39,40] to increase

the freedom of motion of the loop and the contact of A133 and P137, which is thermodynamically favorable. In this particular conformation, V129 seems compatible with M138, that is, the "upward shift" of the β-sheet(128–133) brings A133 to a position where P137 can efficiently interact and allows loop(134–137) to bend deeper, without the C-terminal-side region colliding against loop(116–118) (Figure 8F). As a result, the interaction of A118-P137 is significantly weakened (Figure 7). In contrast, in the mutants with M129, the full extent of deeper bending is not allowed due to steric clash. That may explain why the effects of the I138M mutation were more accentuated in $PrP_{107\text{-}143}$(M129V&I138M) than in $PrP_{107\text{-}143}$(I138M). For example, the proximity score of A120-M/V129 significantly increased in $PrP_{107\text{-}143}$(M129V); moreover, the score in $PrP_{107\text{-}143}$(M129V&I138M) was higher than that in $PrP_{107\text{-}143}$(M129V) by about 300 (Figure 6). Possibly, efficient bending of loop(134–137) in $PrP_{107\text{-}143}$(M129V&I138M) may facilitate further shifting of the β-sheet(128–133) to cause the difference, whereas the bending tended to be hampered by M129 in $PrP_{107\text{-}143}$(I138M) and the effects of M138 could not be fully manifested. The same explanation holds for the different proximity scores for A116-I139 and A117-A133 (Figure 7).

2.6 Influence of A133V mutation on the $PrP_{107\text{-}143}$ amyloid

V136 (in ovine numbering) is one of the scrapie-prone polymorphisms of ovine PrP.[41] In the present model shown in Figure 4A, the corresponding residue of human PrP, A133, faces the same direction as M129; we were therefore interested in whether an A133V mutation would somehow affect the $PrP_{107\text{-}143}$ amyloid structures. The mutant $PrP_{107\text{-}143}$(A133V) appeared to have β-sheet(120–122) and β-sheet(128–133) that were slightly more stable and widely apart than those of the WT overall (Figures 4G and S2), as confirmed by the heatmap patterns (Figure 5). Consistent with this appearance, the distances between the C_α atoms of residues 118 and 133 were very stably maintained at $\sim$ 7 Å (Figure 10), with the proximity score for A118-V133 being significantly higher than that for the WT (Figure 7). The interaction of A118-V133 may cause a significant increase of the proximity scores for

L130-L130 and M134-M134. In the U-shaped loop, the score for V122-M129 was significantly higher and, reciprocally, that for A120-M129 was lower in the A133V mutant than those in the WT, although the decrease was not statistically significant (Figure 6). The proximity scores of interactions in the N-/C-terminal-side regions were also altered: The score for A117-I139 was increased, along with a decrease in the score for A116-I139 (Figure 7). Those alterations could be explained from the viewpoint of the positional relationship between β-sheet(120–122) and β-sheet(128–133), as discussed above (Figure 8E,F). In the A133V mutant, the stable A118-V133 relationship and the stacking interactions of L130 and M134 would fix the positional relationship of the two β-sheets as in the left panel of Figure 8F. This positional relationship would facilitate V122-M129 interaction and keep I139 away from A116 because of the restricted motion range of the C-terminal-side region.

The altered balance of the hydrophobic interactions induced by the A133V mutation did not improve the stability of the amyloid as much as the M129V mutation, despite the stabilized relationships of the two β-sheets; thus, simulations of the present model did not provide any clues to the mechanism by which V136 of ovine PrP facilitates conversion to disease.

2.7 Conclusion about the $\mathbf{PrP_{107\text{-}143}}$ amyloid model

Collectively, the present local structural model of PrP^{Sc} seems to be more compatible with V129 than with M129. This is an example of an amyloid conformation in which differences between methionine and valine affect the structural stability. Another model, which is more compatible with M129 than with V129, is underway.

Reinforcement of a single hydrophobic interaction between the β-sheets induced by mutations, for example, the V122-M129 interaction in $PrP_{107\text{-}143}$(A133V) or A120-V129 interaction in $PrP_{107\text{-}143}$(M129V&I138M) amyloids, did not facilitate stabilization of the local structures. To the contrary, the significantly lowered L125-L125 proximity score of $PrP_{107\text{-}143}$(M129V&I138M) suggests that this alteration causes a certain degree of desta-

bilization of the β-arch (Figure S2D). The results of αSyn(G84M) and $PrP_{107\text{-}143}$(M129V) imply that well-balanced interactions of constituent residues in the hydrophobic core might be essential for maximal stability of a β-arch.

Incidentally, the spontaneous approach of the N- and C-termini of the $PrP_{107\text{-}143}$ amyloid, which occurred with high A/V133-P137 proximity scores, was notable because the N- and C-termini lead to positive- and negative-charge clusters, respectively, in a full-length human PrP. Those charged clusters could electrostatically interact and contribute to the stabilization of the amyloid structures. Interestingly, the positive-charge cluster was previously suggested to be essential for the structural conversion of the N-terminal region.[42]

Knowledge from the present study may help in the design of more plausible PrP^{Sc} models, local structural models of other regions of PrP^{Sc}, and other in-register parallel amyloids. For example, the region between the first and the second α-helices of PrP (residues 155–177), which is likely an interface between the substrate PrP^{C} and template PrP^{Sc} on the C-terminal side,[43] may also form a β-arch. In a disulfide-crosslink scanning experiment, the conversion efficiencies of the series of mutant mouse PrPs into PrP^{Sc} forms by RML/Chandler scrapie suggest that the side chains of residues 165 and 166 (in mouse PrP numbering) are directed outward from a β-arch, forming a loop;[44,45] this supports our view. However, because hydrophobic residues are sparse while there are many asparagine residues in the region, hydrogen bonds might be more important for reinforcement of the β-arch, rather than for hydrophobic effects.

2.8 Potentially generally applicable knowledge from the present study

The unique effects of each group of hydrophobic amino acids in the in-register parallel β-sheet amyloids were conformation-dependent and attributable to C_β-branching and/or the length of the side chains. Methionine and isoleucine showed similar influences in the flat-loop of the αSyn amyloid (E61M and E61I), whereas isoleucine and valine in the U-shaped

loops destabilized the structures when they were not stably incorporated in hydrophobic cores (G84I and G84V). As the latter effects were observed in two different protein models, αSyn(G84I) and $PrP_{107\text{-}143}$(G127V), this notion may be generally applicable to other in-register parallel amyloids. In certain situations, methionine can behave distinctly from other hydrophobic amino acids, as in αSyn(G84M) amyloid, where its long side chain functioned as a crossbeam that ran across the β-arch and stabilized it, forming a well-balanced interaction network. The long hydrophobic side chain of methionine would also be advantageous for efficient inter-domain and intermolecular interactions, as seen in an Aβ amyloid (PDB ID: 2MPZ).[46] However, methionine is not always advantageous for stable hydrophobic core formation, as demonstrated in the M129V mutants of the tentative $PrP_{107\text{-}143}$ amyloid. In terms of C_β-branching and the length of side chains, valine and methionine can have mutually different influences on β-arches, and, if the β-arch constitutes an interface between substrate monomer and template amyloid, such differences would cause species/strain barriers. The influences of an M/V129 polymorphism of human PrP on the phenotypes of prion diseases and susceptibilities to certain prion strains, for example, new-variant CJD,[7,8] might be explainable from this view point.

2.9 Limitations to the present method

A caveat to our hypothesis is the artificial setting for the MD simulation, which starts with the same initial conformations irrespective of mutant types. In reality, the higher freedom of motion of the backbone and potential steric effects of the long side chain of methionine hampered its settling into amyloid conformations. For example, the spontaneous amyloid formation caused by the Y145Stop mutant of Syrian-hamster PrP, which has more methionine than the mouse or human PrP counterparts, is inefficient.[23] Such inefficiency in folding into a conformation may divert a certain fraction of molecules to aberrant refolding pathways in in vitro or in vivo experiments. Regardless of these limitations, MD simulation provides direct insight into the structures and dynamics of in-register parallel β-sheet amyloids, and this

approach would shed light on the mechanisms of the strain diversity of amyloids, including PrP^{Sc}.

3 Conclusion

We have demonstrated how different hydrophobic amino acids uniquely affect the stability of U-shaped β-arches and consequently the entire amyloid in two different in-register parallel β-sheet amyloids. Our studies have also revealed how the manifestations of the effects of one mutation are affected by another mutation. This concept would be applicable to various in-register parallel β-sheet amyloids and other β-arches of PrP^{Sc}. We expect that the knowledge from the present study will aid in the design of more plausible PrP^{Sc} models and other amyloids in the future, in addition to advancing our understanding of in-register parallel β-sheet amyloids.

4 Methods

4.1 Modeling structures of αSyn amyloids

We used a Greek-key αSyn amyloid (PDB ID: 2N0A[33]) as a starting structure, after truncating the disordered N- and C-terminal-side regions (residues 1–35 and 100–140, respectively) (see Figure 1).[29] The N- and C-termini were acetylated and N-methylated using AmberTools16, respectively.[47] For modeling the αSyn mutants, we used SCWRL4.[48] The modeled amyloids were solvated with a rhombic dodecahedron water box with a minimum wall distance of 12 Å using GROMACS (version 5.0.4). Na^+ and Cl^- ions were randomly placed to neutralize the system and yield a net concentration of 150 mM NaCl. The protonation state of the histidine at residue 50 was fixed as the N_δ-H tautomer (HID form in the AMBER naming convention) in all simulations.

4.2 MD simulation of the αSyn amyloids

GROMACS (versions 5.0.4 and 5.1.2)[49] with the AMBER ff99SB-ILDN force field[50] was used for MD simulations with the TIP3P water model.[51] The system was initially minimized for 5,000 steps with the steepest descent method, followed by 2,000 steps with the conjugate gradient method. During minimization, heavy atoms of the amyloids were restrained with a harmonic potential with a force constant of 10.0 kcal/mol $\cdot$ Å^2. After minimization, the system temperature was increased from 0 to 310 K during a 1 ns simulation with the restraints. Next, a 1 ns equilibration run was performed while gradually removing the restraints from 10.0 kcal/mol $\cdot$ Å^2 to zero, and subsequent equilibration was performed in the NPT ensemble for 2 ns at 310 K and 1 bar. The production runs were carried out for 400 ns in the NPT ensemble at 310 K and 1 bar (Figure S4A). We used the velocity-rescaling scheme[52] and the Berendsen scheme[53] for the thermostat and barostat, respectively. The LINCS algorithm[54] was used to constrain all bonds with hydrogen atoms, allowing the use of a 2 fs time-step. Electrostatic interactions were calculated with the Particle-mesh Ewald method.[55] The cut-off length was set to 12 Å for the Coulomb and van der Waals interactions. The Verlet cutoff scheme[56] was used for neighbor-searching. Trajectory snapshots were saved every 10 ps. We conducted five (for WT) and three (for the mutants) independent 400-ns MD simulations.

4.3 Analyses

Backbone root-mean-square deviation (RMSD), RMSF, potential energy, and distance between atoms were calculated using GROMACS.[49] Convergence of the simulations were checked by using backbone RMSD (Figure S5). For the analyses of the 400-ns simulations, the first 100 ns of each MD trajectory was discarded, and 30,001 snapshots (trajectory from 100 to 400 ns) were used (Figure S4A). The secondary structure content during the simulations was calculated with DSSP[57,58] using *gmx do_dssp* in GROMACS. Hydrophobic contacts were analyzed using PyInteraph.[59] A hydrophobic contact was assigned if the distance between the centers of mass of the side chains was less than 5 Å.[38,59] The results

of the hydrophobic contact analyses were visualized using Cytoscape (version 3.5.1).[60] All molecular structures for the αSyn amyloids were drawn with UCSF Chimera (version 1.12)[61] or VMD.[62] Movies of the MD simulation trajectories were prepared with UCSF Chimera.[61]

4.4 Modeling $\mathbf{PrP_{107\text{-}143}}$ amyloids and MD simulations

In designing the local structural models of human PrP^{Sc}, we adopted the region comprising $-GGL_{125}GG-$, as denoted above (see Section 2.2), and avoided charged residues in the N- and C-termini of the peptide because they can excessively destabilize in-register parallel β-sheet structures, particularly when they are at the free ends. There are positive- and negative-charge clusters in regions 101–106 and 144–147, respectively; thus, the region between them was used for the modeling. First, we roughly designed conformations of a single layer of amyloid with Swiss PDB viewer,[63] then piled it up to make an in-register parallel β-sheet amyloid with UCSF Chimera.[61] The model amyloids with 10 layers were refined using Modeller (version 9.15)[64] with β-sheet restraints for the residues A120–V122, Y128–L130, and I138–F141. Mutants were generated by using SCWRL4,[48] and subsequently the N- and C-termini of the refined models were acetylated and N-methylated using PyMOL, respectively.[65] We performed 10 independent 50-ns MD simulations for each model using nearly the same procedure as for the 400-ns MD simulations of αSyn (Figure S4B). We checked convergence of the simulations with backbone RMSD (Figures S6–S11) and potential energy (Figures S12–S17). The last 10 ns of each trajectory (40–50 ns) was analyzed as described in Section 4.3.

4.5 Statistical analyses

Tukey's multiple comparison test ($\alpha = 0.05$) was applied for the statistical analysis with the aid of the *multcomp* package in R.[66] The graphs of the statistical analysis were drawn with the *ggplot2* R package.[67]

Conflict of interest

The authors declare no competing financial interests.

Author contributions

Conceptualization, Y.T.; Methodology, H.O.; Validation, Y.T. and N.N.; Formal Analysis, Y.T. and H.O.; Investigation, H.O. and Y.T.; Resources, H.O. and N.N.; Data Curation, H.O. and Y.T.; Writing (Original Draft Preparation), Y.T.; Writing (Review & Editing), Y.T., H.O., and N.N.; Visualization, H.O. and Y.T.; Supervision, N.N.; Project Administration, Y.T.; Funding Acquisition, H.O., Y.T., and N.N.

Acknowledgement

The numerical calculations were performed on the TSUBAME2.5/3.0 supercomputer at the Tokyo Institute of Technology and the Reedbush supercomputers at the Information Technology Center, the University of Tokyo. HO acknowledges the support of the "TSUBAME Encouragement Program for Young/Female Users" of the Global Scientific Information and Computing Center at the Tokyo Institute of Technology; and the "Initiative on Promotion of Supercomputing for Young or Women Researchers" of the Information Technology Center, the University of Tokyo. This work was supported by a grant from the Takeda Science Foundation (www.takeda-sci.or.jp/) (to YT), and JSPS KAKENHI Grant Numbers 19K16058 (to HO) and 19K22539 (to YT).

Supporting Information Available

The following files are available free of charge.

- SI.pdf: C_α-C_α distance between residues 84 and 89 in the αSyn mutants, final snapshots of MD simulations of $PrP_{107\text{-}143}$, definition of hydrophobic contact and proximity

score, correlations between proximity score and C_α-C_α distance, procedure of MD simulation, time series of backbone RMSD of the αSyn amyloids, time series of backbone RMSD of $PrP_{107\text{-}143}$, time series of potential energy of $PrP_{107\text{-}143}$.

- Movie_S1.mpg: A trajectory of MD simulation of αSyn(G84M). Only residues 82 to 91 are shown. The side chains of M84 and A89 are shown with sticks.
- Movie_S2.mpg: A trajectory of MD simulation of $PrP_{107\text{-}143}$(WT).
- Movie_S3.mpg: A trajectory of MD simulation of $PrP_{107\text{-}143}$(G127V).

References

(1) Prusiner, S. B. Prions. *Proc. Natl. Acad. Sci. U. S. A.* **1998**, *95*, 13363–13383.

(2) Hope, J.; Reekie, L. J. D.; Hunter, N.; Multhaup, G.; Beyreuther, K.; White, H.; Scott, A. C.; Stack, M. J.; Dawson, M.; Wells, G. A. H. Fibrils from brains of cows with new cattle disease contain scrapie-associated protein. *Nature* **1988**, *336*, 390–392.

(3) Williams, E. S. Chronic wasting disease. *Vet. Pathol.* **2005**, *42*, 530–549.

(4) Telling, G. C.; Parchi, P.; DeArmond, S. J.; Cortelli, P.; Montagna, P.; Gabizon, R.; Mastrianni, J.; Lugaresi, E.; Gambetti, P.; Prusiner, S. B. Evidence for the conformation of the pathologic isoform of the prion protein enciphering and propagating prion diversity. *Science* **1996**, *274*, 2079–2082.

(5) Parchi, P. et al. Classification of sporadic Creutzfeldt-Jakob disease based on molecular and phenotypic analysis of 300 subjects. *Ann. Neurol.* **1999**, *46*, 224–233.

(6) Goldfarb, L. G.; Petersen, R. B.; Tabaton, M.; Brown, P.; LeBlanc, A. C.; Montagna, P.; Cortelli, P.; Julien, J.; Vital, C.; Pendelbury, W. W. Fatal familial insomnia and familial Creutzfeldt-Jakob disease: disease phenotype determined by a DNA polymorphism. *Science* **1992**, *258*, 806–808.

(7) Collinge, J.; Beck, J.; Campbell, T.; Estibeiro, K.; Will, R. G. Prion protein gene analysis in new variant cases of Creutzfeldt-Jakob disease. *Lancet* **1996**, *348*, 56.

(8) Collinge, J. Molecular neurology of prion disease. *J. Neurol. Neurosurg. Psychiatry* **2005**, *76*, 906–919.

(9) Green, K. M.; Browning, S. R.; Seward, T. S.; Jewell, J. E.; Ross, D. L.; Green, M. A.; Williams, E. S.; Hoover, E. A.; Telling, G. C. The elk PRNP codon 132 polymorphism controls cervid and scrapie prion propagation. *J. Gen. Virol.* **2008**, *89*, 598–608.

(10) Hamir, A. N.; Gidlewski, T.; Spraker, T. R.; Miller, J. M.; Creekmore, L.; Crocheck, M.; Cline, T.; O'Rourke, K. I. Preliminary observations of genetic susceptibility of elk (Cervus Elaphus Nelsoni) to chronic wasting disease by experimental oral inoculation. *J. Vet. Diagn. Invest.* **2006**, *18*, 110–114.

(11) Vázquez-Fernández, E.; Vos, M. R.; Afanasyev, P.; Cebey, L.; Sevillano, A. M.; Vidal, E.; Rosa, I.; Renault, L.; Ramos, A.; Peters, P. J.; Fernández, J. J.; van Heel, M.; Young, H. S.; Requena, J. R.; Wille, H. The structural architecture of an infectious mammalian prion using electron cryomicroscopy. *PLoS Pathog.* **2016**, *12*, e1005835.

(12) Silva, C. J.; Vázquez-Fernández, E.; Onisko, B.; Requena, J. R. Proteinase K and the structure of PrP^{Sc}: The good, the bad and the ugly. *Virus Res.* **2015**, *207*, 120–126.

(13) Tycko, R.; Savtchenko, R.; Ostapchenko, V. G.; Makarava, N.; Baskakov, I. V. The α-helical C-terminal domain of full-length recombinant PrP converts to an in-register parallel β-sheet structure in PrP fibrils: evidence from solid state nuclear magnetic resonance. *Biochemistry* **2010**, *49*, 9488–9497.

(14) Groveman, B. R.; Dolan, M. A.; Taubner, L. M.; Kraus, A.; Wickner, R. B.; Caughey, B. Parallel in-register intermolecular β-sheet architectures for prion-seeded prion protein (PrP) amyloids. *J. Biol. Chem.* **2014**, *289*, 24129–24142.

(15) Cobb, N. J.; Sönnichsen, F. D.; Mchaourab, H.; Surewicz, W. K. Molecular architecture of human prion protein amyloid: A parallel, in-register β-structure. *Proc. Natl. Acad. Sci. U. S. A.* **2007**, *104*, 18946–18951.

(16) Theint, T.; Xia, Y.; Nadaud, P. S.; Mukhopadhyay, D.; Schwieters, C. D.; Surewicz, K.; Surewicz, W. K.; Jaroniec, C. P. Structural studies of amyloid fibrils by paramagnetic solid-state nuclear magnetic resonance spectroscopy. *J. Am. Chem. Soc.* **2018**, *140*, 13161–13166.

(17) Spagnolli, G.; Rigoli, M.; Orioli, S.; Sevillano, A. M.; Faccioli, P.; Wille, H.; Biasini, E.; Requena, J. R. Full atomistic model of prion structure and conversion. *PLoS Pathog.* **2019**, *15*, e1007864.

(18) Baskakov, I. V.; Caughey, B.; Requena, J. R.; Sevillano, A. M.; Surewicz, W. K.; Wille, H. The prion 2018 round tables (I): the structure of PrP^{Sc}. *Prion* **2019**, *13*, 46–52.

(19) Priola, S. A.; Chesebro, B. A single hamster PrP amino acid blocks conversion to protease-resistant PrP in scrapie-infected mouse neuroblastoma cells. *J. Virol.* **1995**, *69*, 7754–7758.

(20) Vanik, D. L.; Surewicz, K. A.; Surewicz, W. K. Molecular basis of barriers for interspecies transmissibility of mammalian prions. *Mol. Cell* **2004**, *14*, 139–145.

(21) Giles, K.; De Nicola, G. F.; Patel, S.; Glidden, D. V.; Korth, C.; Oehler, A.; DeArmond, S. J.; Prusiner, S. B. Identification of I137M and other mutations that modulate incubation periods for two human prion strains. *J. Virol.* **2012**, *86*, 6033–6041.

(22) Lowenstein, D. H.; Butler, D. A.; Westaway, D.; McKinley, M. P.; DeArmond, S. J.; Prusiner, S. B. Three hamster species with different scrapie incubation times and neuropathological features encode distinct prion proteins. *Mol. Cell. Biol.* **1990**, *10*, 1153–1163.

(23) Meade-White, K. D.; Barbian, K. D.; Race, B.; Favara, C.; Gardner, D.; Taubner, L.; Porcella, S.; Race, R. Characteristics of 263K scrapie agent in multiple hamster species. *Emerg. Infect. Dis.* **2009**, *15*, 207–215.

(24) Harrathi, C.; Fernández-Borges, N.; Eraña, H.; Elezgarai, S. R.; Venegas, V.; Charco, J. M.; Castilla, J. Insights into the Bidirectional Properties of the Sheep – Deer Prion Transmission Barrier. *Mol. Neurobiol.* **2019**, *56*, 5287–5303.

(25) Theint, T.; Nadaud, P. S.; Aucoin, D.; Helmus, J. J.; Pondaven, S. P.; Surewicz, K.; Surewicz, W. K.; Jaroniec, C. P. Species-dependent structural polymorphism of Y145Stop prion protein amyloid revealed by solid-state NMR spectroscopy. *Nat. Commun.* **2017**, *8*, 753.

(26) Requena, J. R. The protean prion protein. *PLoS Biol.* **2020**, *18*, e3000754.

(27) Choi, J.-K.; Cali, I.; Surewicz, K.; Kong, Q.; Gambetti, P.; Surewicz, W. K. Amyloid fibrils from the N-terminal prion protein fragment are infectious. *Proc. Natl. Acad. Sci. U. S. A.* **2016**, *113*, 13851–13856.

(28) Taguchi, Y.; Otaki, H.; Nishida, N. Mechanisms of strain diversity of disease-associated in-register parallel β-sheet amyloids and implications about prion strains. *Viruses* **2019**, *11*, 110.

(29) Otaki, H.; Taguchi, Y.; Nishida, N. Molecular dynamics simulation reveals that switchable combinations of β-sheets underlie the prion-like properties of α-synuclein amyloids. *bioRxiv* **2018**, *326462*.

(30) Melki, R. Alpha-synuclein and the prion hypothesis in Parkinson's disease. *Rev. Neurol. (Paris)* **2018**, *174*, 644–652.

(31) Bousset, L.; Pieri, L.; Ruiz-Arlandis, G.; Gath, J.; Jensen, P. H.; Habenstein, B.; Ma-

diona, K.; Olieric, V.; Böckmann, A.; Meier, B. H.; Melki, R. Structural and functional characterization of two alpha-synuclein strains. *Nat. Commun.* **2013**, *4*, 2575.

(32) Peng, C.; Gathagan, R. J.; Covell, D. J.; Medellin, C.; Stieber, A.; Robinson, J. L.; Zhang, B.; Pitkin, R. M.; Olufemi, M. F.; Luk, K. C.; Trojanowski, J. Q.; Lee, V. M. Y. Cellular milieu imparts distinct pathological α-synuclein strains in α-synucleinopathies. *Nature* **2018**, *557*, 558–563.

(33) Tuttle, M. D. et al. Solid-state NMR structure of a pathogenic fibril of full-length human α-synuclein. *Nat. Struct. Mol. Biol.* **2016**, *23*, 409–415.

(34) Li, B.; Ge, P.; Murray, K. A.; Sheth, P.; Zhang, M.; Nair, G.; Sawaya, M. R.; Shin, W. S.; Boyer, D. R.; Ye, S.; Eisenberg, D. S.; Zhou, Z. H.; Jiang, L. Cryo-EM of full-length α-synuclein reveals fibril polymorphs with a common structural kernel. *Nat. Commun.* **2018**, *9*, 3609.

(35) Guerrero-Ferreira, R.; Taylor, N. M. I.; Mona, D.; Ringler, P.; Lauer, M. E.; Riek, R.; Britschgi, M.; Stahlberg, H. Cryo-EM structure of alpha-synuclein fibrils. *eLife* **2018**, *7*, e36402.

(36) Asante, E. A. et al. A naturally occurring variant of the human prion protein completely prevents prion disease. *Nature* **2015**, *522*, 478–481.

(37) Glynn, C.; Sawaya, M. R.; Ge, P.; Gallagher-Jones, M.; Short, C. W.; Bowman, R.; Apostol, M.; Zhou, Z. H.; Eisenberg, D. S.; Rodriguez, J. A. Cryo-EM structure of a human prion fibril with a hydrophobic, protease-resistant core. *Nat. Struct. Mol. Biol.* **2020**, *27*, 417–423.

(38) Salamanca Viloria, J.; Allega, M. F.; Lambrughi, M.; Papaleo, E. An optimal distance cutoff for contact-based Protein Structure Networks using side-chain centers of mass. *Sci. Rep.* **2017**, *7*, 2838.

(39) Lyu, P. C.; Sherman, J. C.; Chen, A.; Kallenbach, N. R. α-Helix stabilization by natural and unnatural amino acids with alkyl side chains. *Proc. Natl. Acad. Sci. U. S. A.* **1991**, *88*, 5317–5320.

(40) Berg, J. M.; Tymoczko, J. L.; Stryer, L. *Biochemistry*, 5th ed.; W H Freeman: New York, 2002.

(41) Goldmann, W.; Hunter, N.; Smith, G.; Foster, J.; Hope, J. PrP Genotype and agent effects in scrapie: change in allelic interaction with different isolates of agent in sheep, a natural host of scrapie. *J. Gen. Virol.* **1994**, *75*, 989–995.

(42) Groveman, B. R.; Raymond, G. J.; Campbell, K. J.; Race, B.; Raymond, L. D.; Hughson, A. G.; Orrú, C. D.; Kraus, A.; Phillips, K.; Caughey, B. Role of the central lysine cluster and scrapie templating in the transmissibility of synthetic prion protein aggregates. *PLoS Pathog.* **2017**, *13*, e1006623.

(43) Taguchi, Y.; Mistica, A. M. A.; Kitamoto, T.; Schätzl, H. M. Critical significance of the region between Helix 1 and 2 for efficient dominant-negative inhibition by conversion-incompetent prion protein. *PLoS Pathog.* **2013**, *9*, e1003466.

(44) Taguchi, Y.; Lu, L.; Marrero-Winkens, C.; Otaki, H.; Nishida, N.; Schatzl, H. M. Disulfide-crosslink scanning reveals prion-induced conformational changes and prion strain-specific structures of the pathological prion protein PrP^{Sc}. *J. Biol. Chem.* **2018**, *293*, 12730–12740.

(45) Taguchi, Y.; Lu, L.; Marrero-Winkens, C.; Otaki, H.; Nishida, N.; Schatzl, H. M. Correction: Disulfide-crosslink scanning reveals prion-induced conformational changes and prion strain-specific structures of the pathological prion protein PrP^{Sc}. *J. Biol. Chem.* **2018**, *293*, 14925.

(46) Sgourakis, N.; Yau, W.-M.; Qiang, W. Modeling an in-register, parallel "Iowa" Aβ fibril

structure using solid-state NMR data from labeled samples with Rosetta. *Structure* **2015**, *23*, 216–227.

(47) Case, D. et al. AmberTools16. 2016.

(48) Krivov, G. G.; Shapovalov, M. V.; Dunbrack, R. L. Improved prediction of protein side-chain conformations with SCWRL4. *Proteins* **2009**, *77*, 778–795.

(49) Abraham, M. J.; Murtola, T.; Schulz, R.; Páll, S.; Smith, J. C.; Hess, B.; Lindahl, E. GROMACS: High performance molecular simulations through multi-level parallelism from laptops to supercomputers. *SoftwareX* **2015**, *1-2*, 19–25.

(50) Lindorff-Larsen, K.; Piana, S.; Palmo, K.; Maragakis, P.; Klepeis, J. L.; Dror, R. O.; Shaw, D. E. Improved side-chain torsion potentials for the Amber ff99SB protein force field. *Proteins* **2010**, *78*, 1950–1958.

(51) Jorgensen, W. L.; Chandrasekhar, J.; Madura, J. D.; Impey, R. W.; Klein, M. L. Comparison of simple potential functions for simulating liquid water. *J. Chem. Phys.* **1983**, *79*, 926–935.

(52) Bussi, G.; Donadio, D.; Parrinello, M. Canonical sampling through velocity rescaling. *J. Chem. Phys.* **2007**, *126*, 014101.

(53) Berendsen, H. J. C.; Postma, J. P. M.; van Gunsteren, W. F.; DiNola, A.; Haak, J. R. Molecular dynamics with coupling to an external bath. *J. Chem. Phys.* **1984**, *81*, 3684–3690.

(54) Hess, B. P-LINCS: A parallel linear constraint solver for molecular simulation. *J. Chem. Theory Comput.* **2008**, *4*, 116–122.

(55) Essmann, U.; Perera, L.; Berkowitz, M. L.; Darden, T.; Lee, H.; Pedersen, L. G. A smooth particle mesh Ewald method. *J. Chem. Phys.* **1995**, *103*, 8577–8593.

(56) Páll, S.; Hess, B. A flexible algorithm for calculating pair interactions on SIMD architectures. *Comput. Phys. Commun.* **2013**, *184*, 2641–2650.

(57) Touw, W. G.; Baakman, C.; Black, J.; te Beek, T. A. H.; Krieger, E.; Joosten, R. P.; Vriend, G. A series of PDB-related databanks for everyday needs. *Nucleic Acids Res.* **2015**, *43*, D364–D368.

(58) Kabsch, W.; Sander, C. Dictionary of protein secondary structure: Pattern recognition of hydrogen-bonded and geometrical features. *Biopolymers* **1983**, *22*, 2577–2637.

(59) Tiberti, M.; Invernizzi, G.; Lambrughi, M.; Inbar, Y.; Schreiber, G.; Papaleo, E. Py-Interaph: A framework for the analysis of interaction networks in structural ensembles of proteins. *J. Chem. Inf. Model.* **2014**, *54*, 1537–1551.

(60) Shannon, P.; Markiel, A.; Ozier, O.; Baliga, N. S.; Wang, J. T.; Ramage, D.; Amin, N.; Schwikowski, B.; Ideker, T. Cytoscape: A software environment for integrated models of biomolecular interaction networks. *Genome Res.* **2003**, *13*, 2498–2504.

(61) Pettersen, E. F.; Goddard, T. D.; Huang, C. C.; Couch, G. S.; Greenblatt, D. M.; Meng, E. C.; Ferrin, T. E. UCSF Chimera—A visualization system for exploratory research and analysis. *J. Comput. Chem.* **2004**, *25*, 1605–1612.

(62) Humphrey, W.; Dalke, A.; Schulten, K. VMD: Visual molecular dynamics. *J. Mol. Graph.* **1996**, *14*, 33–38.

(63) Guex, N.; Peitsch, M. C. SWISS-MODEL and the Swiss-Pdb Viewer: An environment for comparative protein modeling. *Electrophoresis* **1997**, *18*, 2714–2723.

(64) Šali, A.; Blundell, T. L. Comparative protein modelling by satisfaction of spatial restraints. *J. Mol. Biol.* **1993**, *234*, 779–815.

(65) DeLano, W. L. Pymol: An open-source molecular graphics tool. *CCP4 Newsletter On Protein Crystallography* **2002**, *40*, 82–92.

(66) Hothorn, T.; Bretz, F.; Westfall, P. Simultaneous inference in general parametric models. *Biom. J.* **2008**, *50*, 346–363.

(67) Wickham, H. *ggplot2: Elegant Graphics for Data Analysis*; Springer-Verlag: New York, 2016.

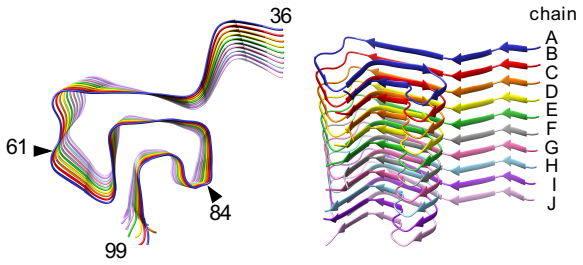

Figure 1: Structure of the Greek-key αSyn amyloid (PDB ID: 2N0A), in which the N- and C-terminal-side regions (residues 1–35 and 100–140, respectively) are truncated. The black triangles indicate the positions of residues 61 and 84. The chains of the amyloid stack are referred to as chains A–J.

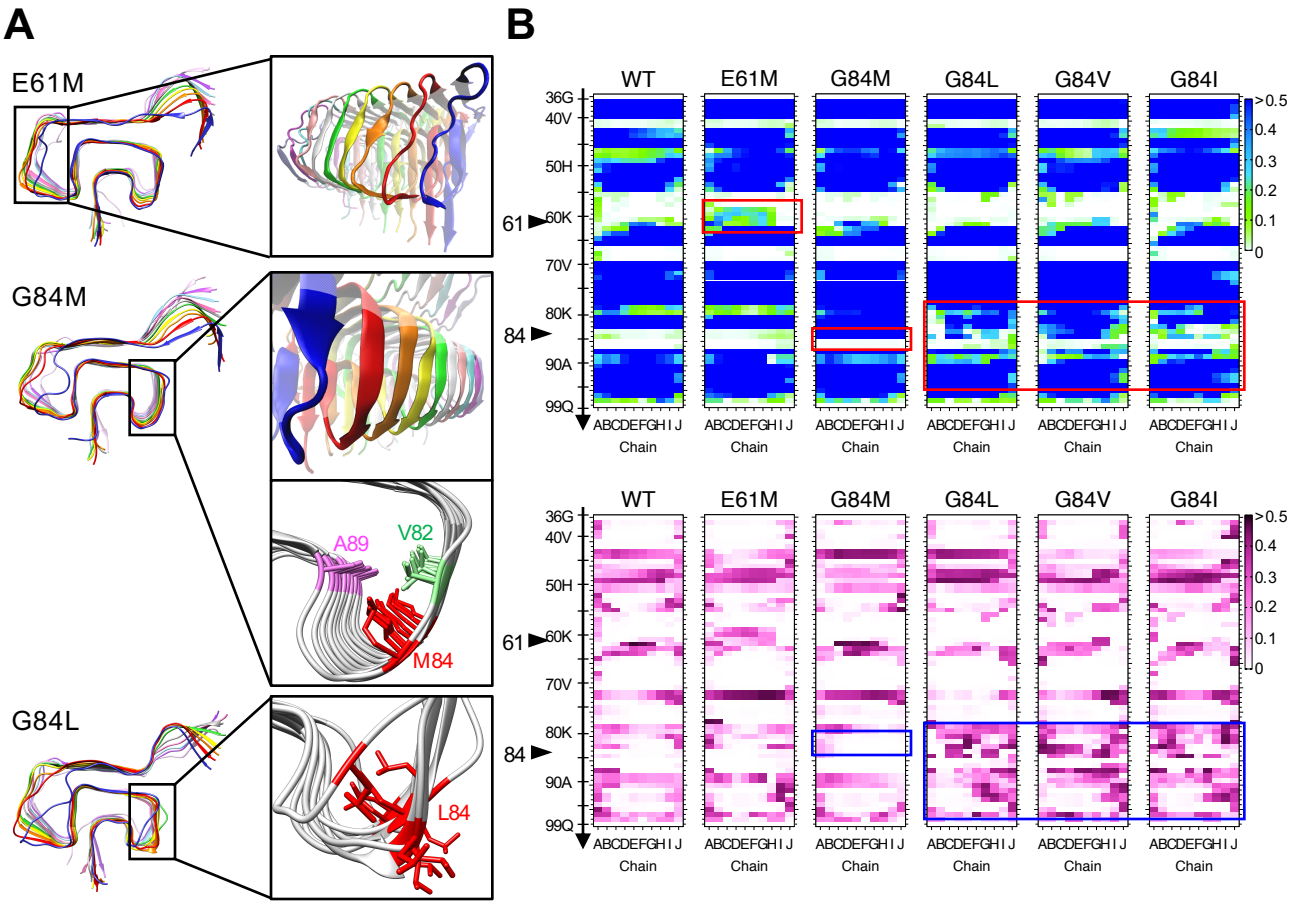

Figure 2: Influences of E61M and G84M/L/V/I substitutions on the local structures of Greek-key αSyn amyloid: (A) Final snapshots of αSyn(E61M), αSyn(G84M), and αSyn(G84L) amyloids after 400-ns MD simulations. The insets present magnified views of the indicated regions. Note that the β-sheets are induced in loop(57–62) of the αSyn(E61M) amyloid and that the αSyn(G84M) amyloid has β-sheets extended to loop(84–87). In αSyn(G84M) and αSyn(G84L), the directions of the side chains of residue 84 after a 400-ns MD simulation are shown with red sticks in the insets. In the inset of αSyn(G84M), the side chains of V82 and A89 are also shown with green and pink sticks, respectively. They were close to the side chains of M84 and forming hydrophobic contacts (see also Figure 3). In αSyn(G84L), the local structures around the mutation were disturbed. Some side chains of L84 are pointing outward, whereas those of M84 remain inside in αSyn(G84M). (B) Heatmaps of the average β-sheet propensity values (Avg-β) and the standard deviation of the values (SD-β) based on five (for WT) and three (for the mutants) independent 400-ns MD simulations. The vertical axes and horizontal axes of all the heatmaps represent the residue numbers and the chains A–J, respectively. The black triangles indicate the positions of residues 61 and 84. Avg-β values in loop(57–62) of αSyn(E61M) and loop(84–87) of the αSyn(G84M) amyloids increased (E61M and G84M, red boxes), corresponding to the induced β-sheets in those regions (see (A)). The relatively low SD-β values in the αSyn(G84M) amyloid (G84M, blue box) reflect the stabilized local structures. In αSyn(G84L), αSyn(G84V), and αSyn(G84I), the structural disturbances caused by the mutation are reflected to the heatmap (G84L/V/I, red and blue boxes). The heatmaps of the WT and G84I mutant are taken from Taguchi et al. (2019),[28] which is published under the CC-BY 4.0 license.

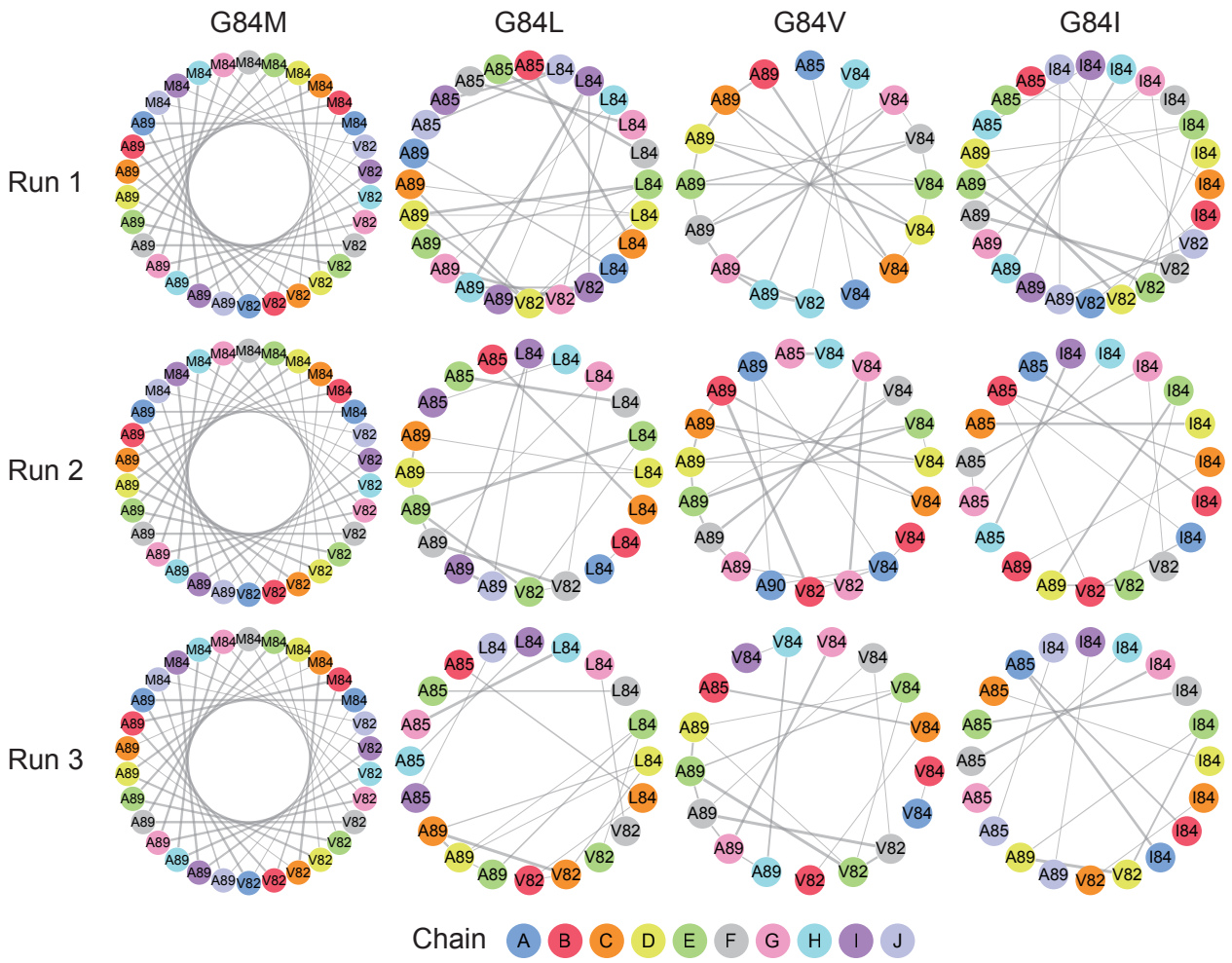

Figure 3: Hydrophobic contact diagrams based on 400-ns simulations of αSyn amyloids. Only the residues involved in the interactions with residue 84 are presented. Residue numbers and chains are indicated by the numbers and colors of the dots, respectively. The thickness of each line corresponds to the occupancy of the hydrophobic contact.

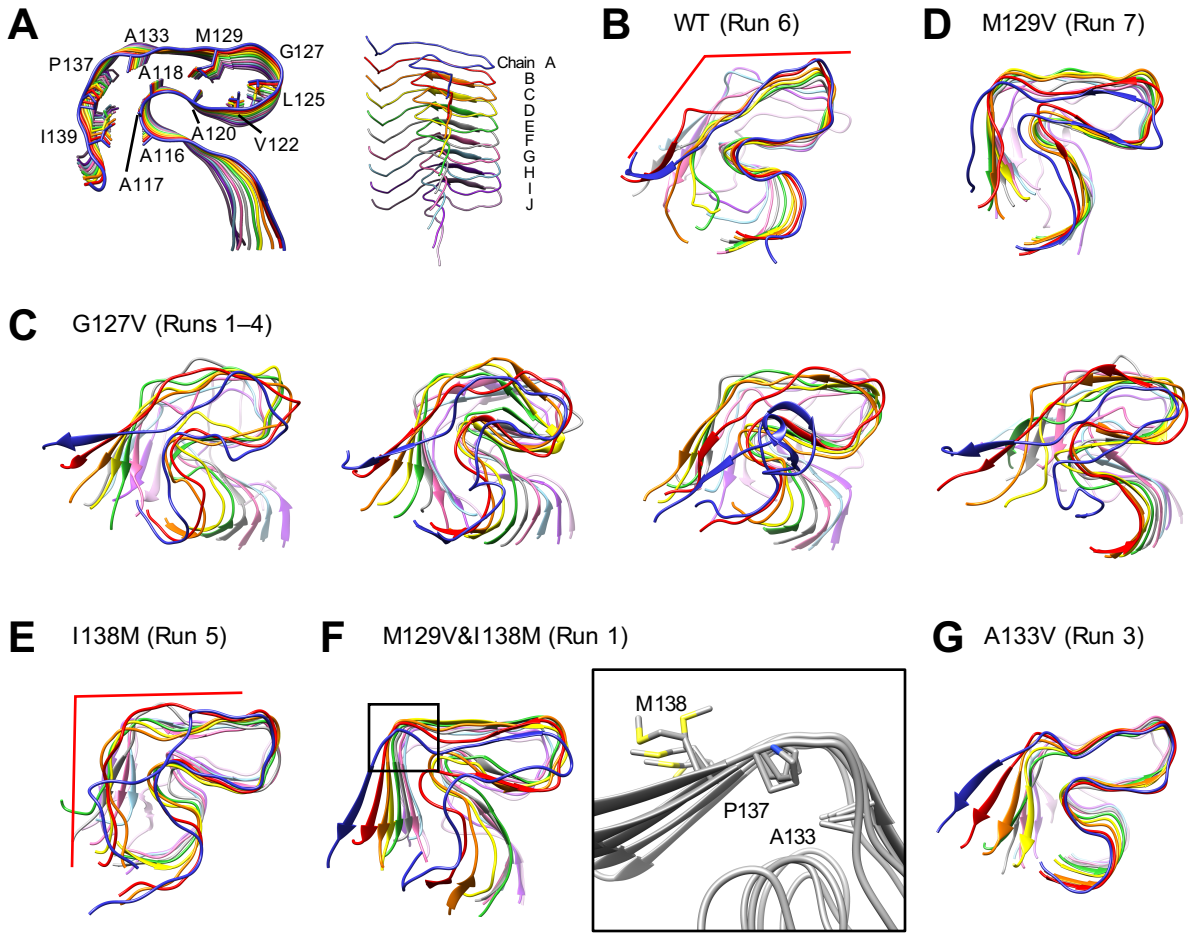

Figure 4: Local-structural model of PrP^{Sc}, $PrP_{107\text{-}143}$, and final snapshots of 50-ns MD simulations. For all the snapshots of 10 runs (except for G127V), see Figure S2: (A) A $PrP_{107\text{-}143}$ amyloid as a tentative local-structural model of PrP^{Sc} and an oblique view showing the 10 layers (chains A–J). Side chains of the residues that are mentioned later are annotated. (B) A final snapshot of WT $PrP_{107\text{-}143}$ (Run 6). (C) Final snapshots of $PrP_{107\text{-}143}$(G127V) in four consecutive runs (Runs 1–4). (D) A final snapshot of $PrP_{107\text{-}143}$(M129V) (Run 7). (E) A final snapshot of $PrP_{107\text{-}143}$(I138M) (Run 5). (F) (Left) A final snapshot of $PrP_{107\text{-}143}$(M129V&I138M) (Run 1). The box indicates Ω-shaped loops encompassing A133 to P137. (Right) Positional relationships of the side chains of A133, P137, and M138 in chains B–F. (G) A final snapshot of $PrP_{107\text{-}143}$(A133V) (Run 3).

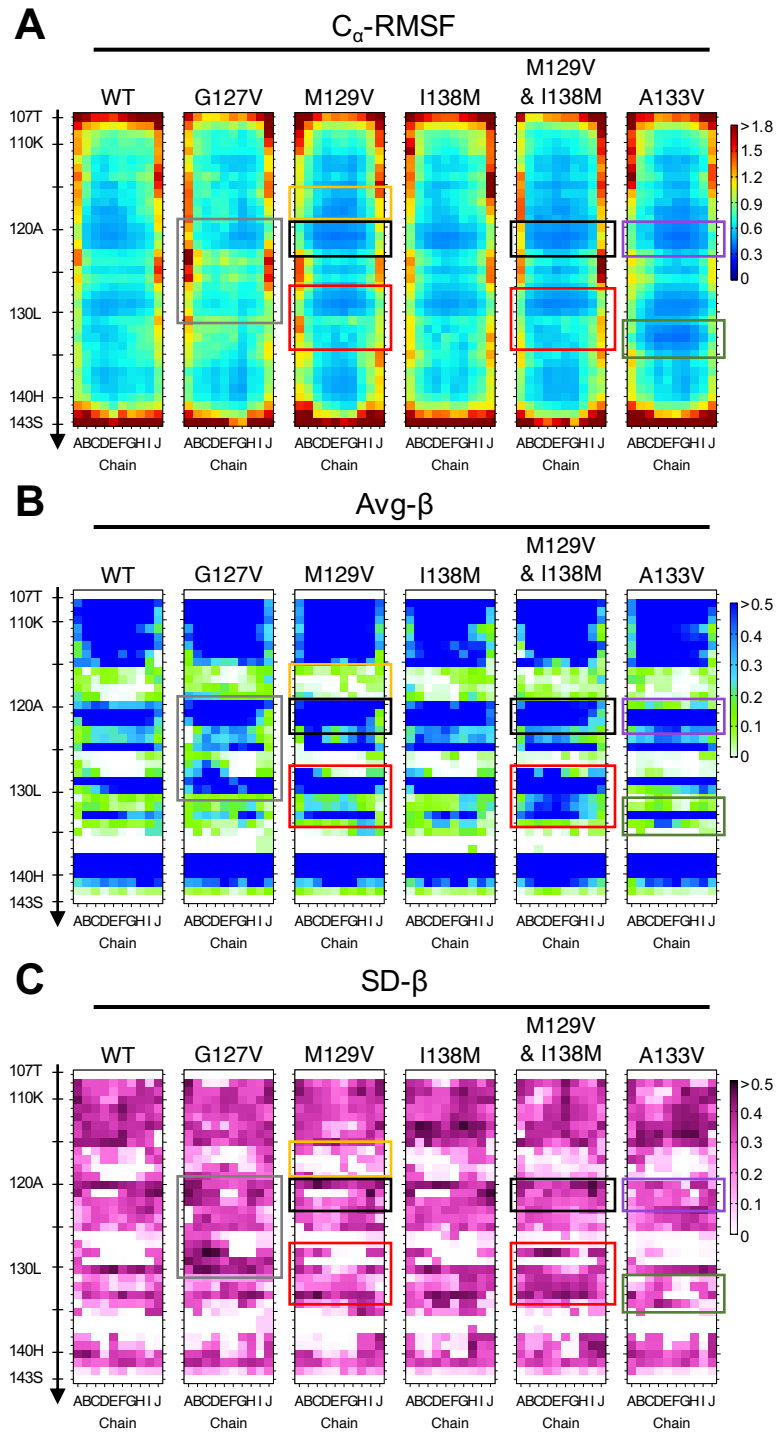

Figure 5: Heatmaps showing (A) the average of root-mean-square fluctuation (RMSF) of C_α atoms, (B) the Avg-β, and (C) the SD-β of each residue of the WT and the mutant $PrP_{107\text{-}143}$ amyloids. The values were calculated from 10 independent 50-ns MD runs: Gray boxes, a disordered loop(120–130); Yellow boxes, a more demarcated loop(116–119, especially chains A–E) than in the WT; Black boxes, a more stable β-sheet(120–122) with higher β-sheet propensity and lower RMSF values than in the WT; Red boxes, a more stable β-sheet(128–133) with lower RMSF and higher β-sheet propensity around L130 than in the WT. Higher SD-β values at A133 are induced by "upward shift" (see Figure 8E,F); Purple boxes, a slightly more stable β-sheet(120–122) with lower RMSF values than in the WT; Green boxes, a higher β-sheet propensity at V133 with lower RMSF and SD-β values than in the WT.

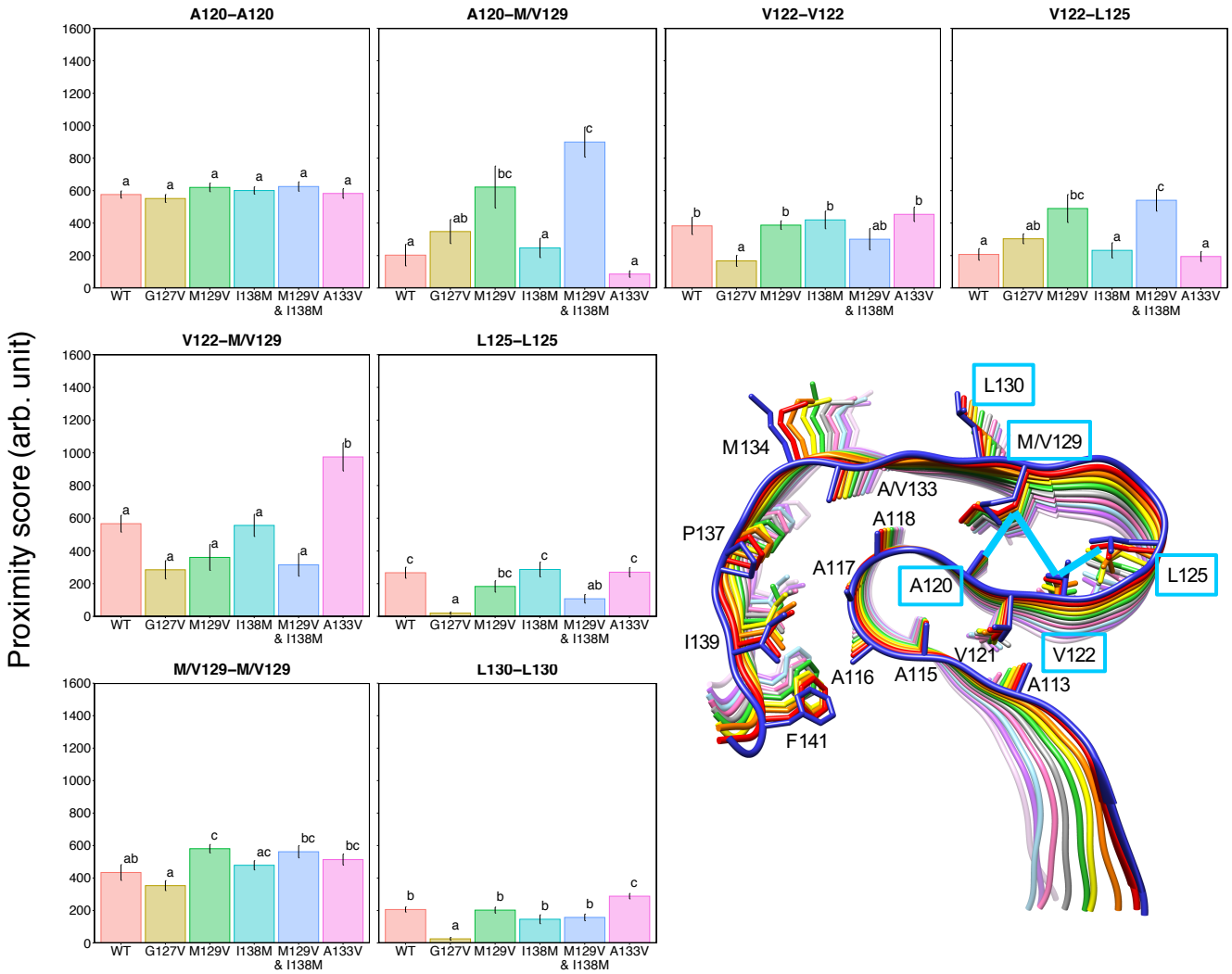

Figure 6: Bar plots of proximity scores between two residues in the U-shaped loop (residues 120–130). The error bar represents the standard error (SE) of the mean of values from 10 independent MD runs. Bars sharing the same letter are not significantly different according to Tukey's test with $\alpha = 0.05$. In the figure of the $PrP_{107\text{-}143}$ amyloid, plotted interactions are represented with light-blue boxed residues (for hydrophobic contacts along the stacking direction) or lines (for the others).

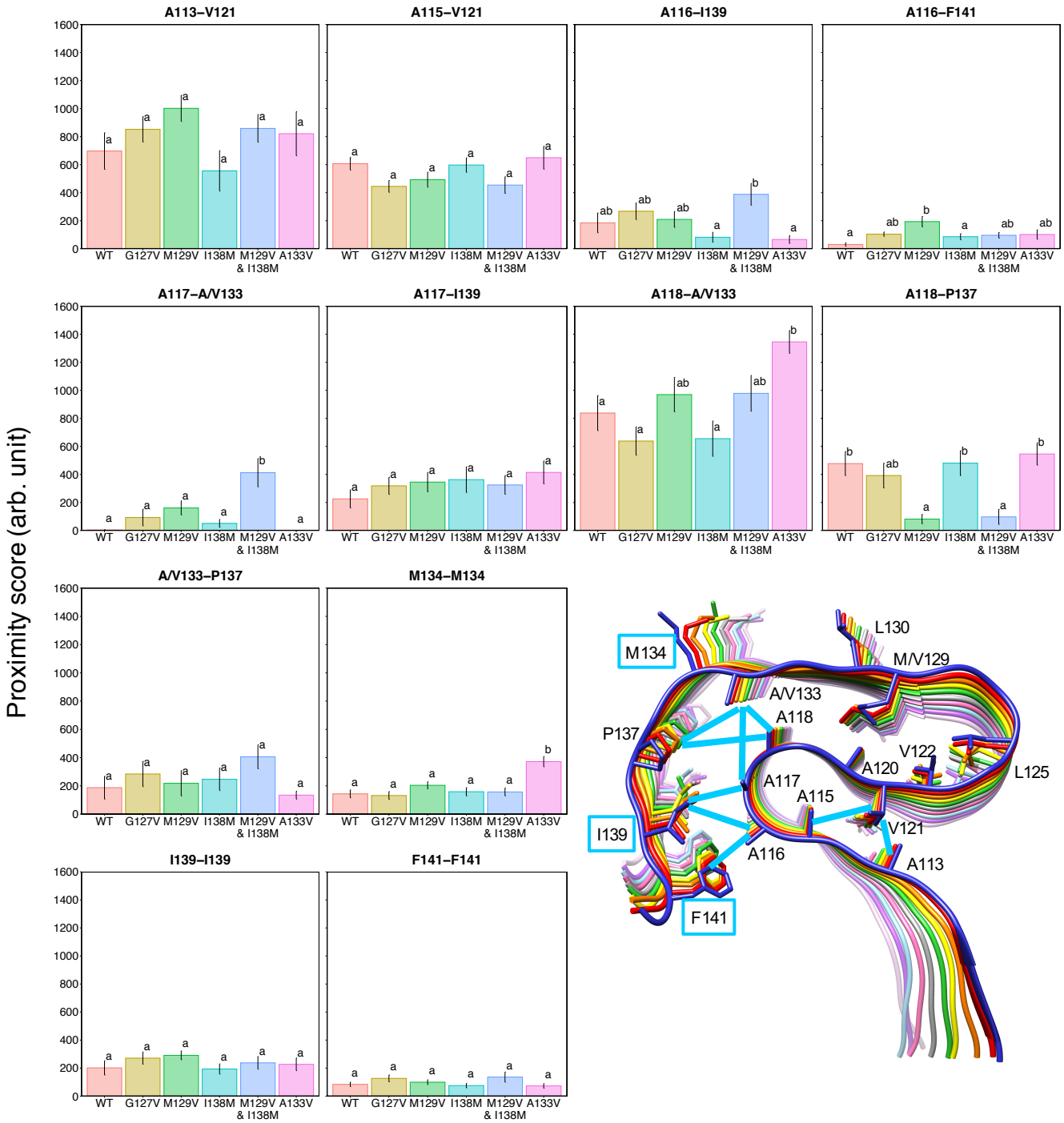

Figure 7: Identical to Figure 6, except for the residues in the N- and C-terminal-side regions.

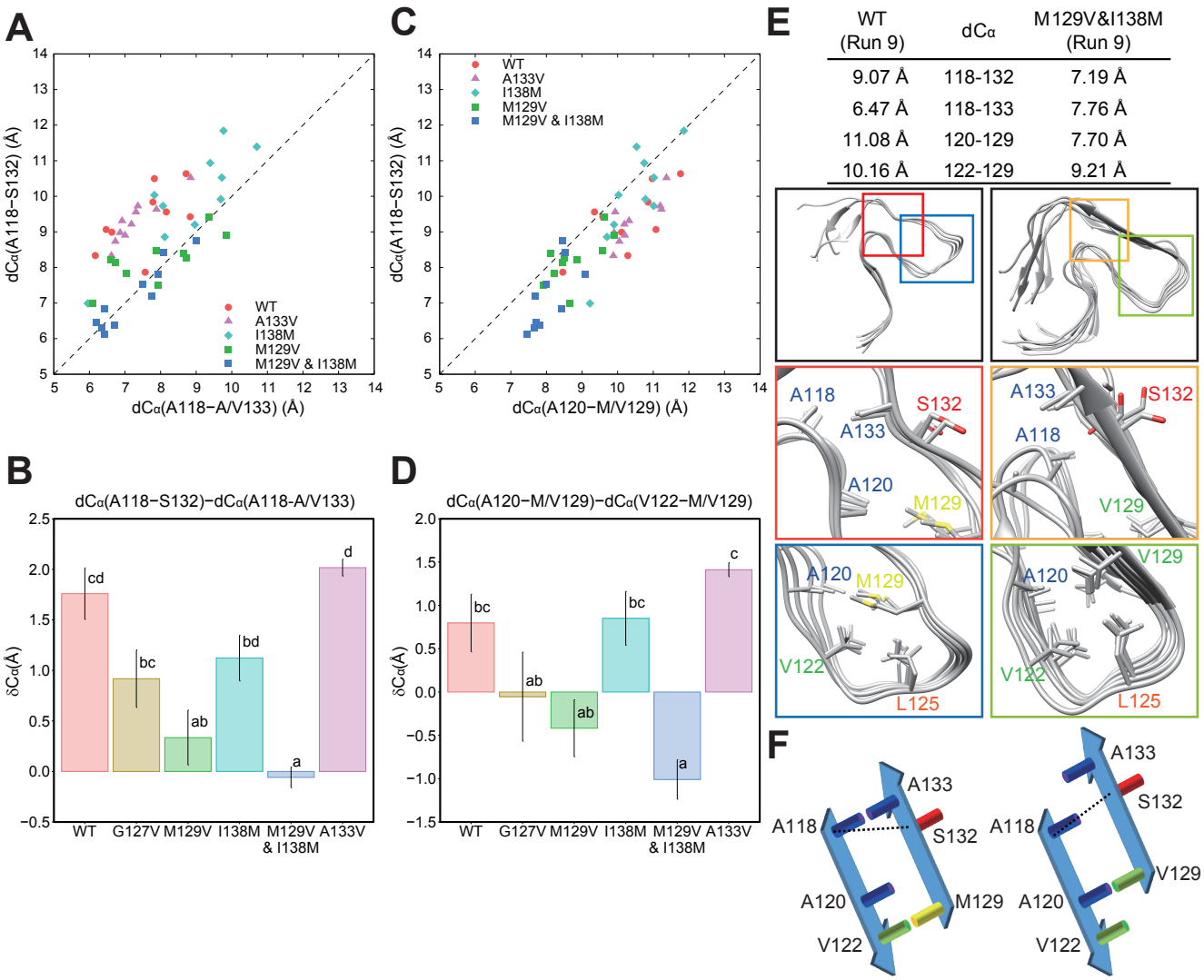

Figure 8: (A) Scatter plot showing correlations of the final C_α-C_α distances for A118-A/V133 (dC_α(A118-A/V133)) and A118-S132 (dC_α(A118-S132)) in the WT and mutant $PrP_{107\text{-}143}$ amyloids. The dashed line is merely a guide for the eye. (B) Bar plot of the difference between the final C_α-C_α distances, δC_α, for dC_α(A118-S132) and dC_α(A118-A/V133) in the WT and mutant $PrP_{107\text{-}143}$ amyloids. The bars and error bars represent the mean $\pm$ standard error (SE) of values obtained from 10 independent MD runs. Bars sharing the same letter are not significantly different according to Tukey's test with $\alpha = 0.05$. (C) Identical to (A), except for dC_α(A120-M/V129) and dC_α(A118-S132). Note that the dC_α(A120-M/V129) values of $PrP_{107\text{-}143}$ with M129V mutations (green and blue squares) are shorter than 9 Å in most of the MD runs and their dC_α(A118-S132) values also tend to be shorter than those of the other mutants. (D) Identical to (B), except for the difference between dC_α(A120-M/V129) and dC_α(V122-M/V129). (E) Final snapshots of the chains D–G of $PrP_{107\text{-}143}$(WT) and chains C–H of $PrP_{107\text{-}143}$(M129V&I138M) after 50-ns MD simulations. The upper table shows dC_α between the residues averaged over chains A–J. The insets show magnified views with the side chains of the residues involved in hydrophobic interactions. (F) A schematic illustration of the positional relationships and "upward shift" of the β-sheet(128–133) induced by the M129V mutation. The dashed lines indicate distances between the C_α atoms of A118 and S132.

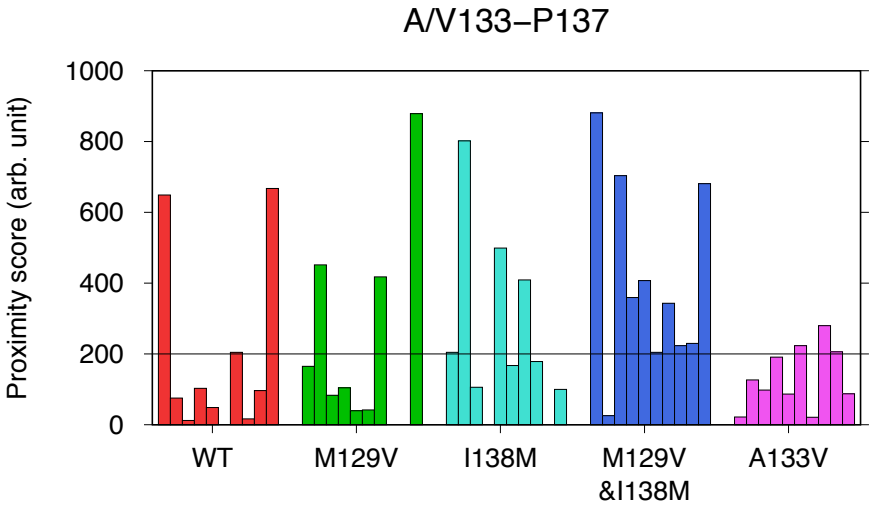

Figure 9: Proximity scores for A/V133-P137. Each bar represents the value obtained from one of the 10 runs (Runs 1 to 10, from left to right). The line at 200 is merely a guide for the eye.

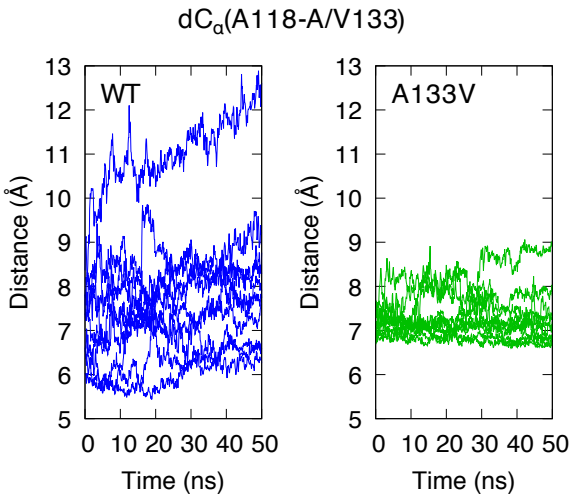

Figure 10: Fluctuations in the average distance between C_α atoms of A118 and A/V133, dC_α(A118-A/V133). Each line represents the average of the distances over chains A–J in each of the 10 MD runs.
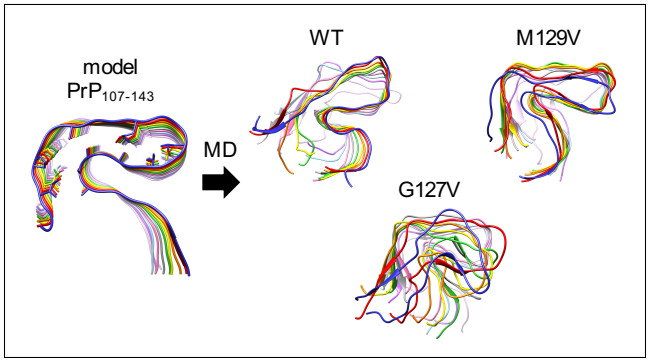
Graphical TOC Entry